a unified tissue-segmentation procedure after correction of image-intensity nonuniformity. Segmented images are then normalized to the MNI (Montreal Neurological Institute) space via a nonlinear transformation to a customized template created by DARTEL, modulation by the Jacobian determinant, and linear transformation from the customized template to MNI space. Finally, the images are smoothed using an 8-mm full-width-at-half-maximum Gaussian kernel. To perform Z-score analysis for gray matter, brain images of 80 healthy control volunteers without memory impairment or cognitive disorders (37 men and 43 women, 70.4 ± 7.8 years of age) were processed using the above procedures, and the mean and standard deviation of these smoothed modulated intensity values were calculated voxel by voxel in MNI space, preliminarily. Finally, a Z-score map was generated by comparing an individual image with a control mean and standard deviation at each voxel in a gray/white matter image. The Z-score was calculated as [control mean] − [individual value]/(control SD) and it shows atrophy relative to the normal control.

Directly assessing the usefulness of VBM analysis is difficult because the true brain atrophy of the subject is unknown. Therefore, we assumed that geometric distortion reduces the reproducibility of the Z-score. Segmentation and anatomical standardization errors may be increased by an anatomical volume change and partial volume effects resulting from distortion. We assessed the reproducibility of VBM analysis for brain images corrected using the J-ADNI method for 38 healthy volunteers (32 men and six women, 33.6 ± 10.7 years of age) scanned twice at an interval of 1 week. The phantom image was obtained immediately after each volunteer was scanned and the imaging sequence is identical with phantom scanning as described in Table I. Using the automated VBM software, we obtained two indicators for characterizing atrophy in medial temporal structures and in the whole brain.[8] The first indicator was the averaged Z-score in the medial temporal structures, which indicates the severity of atrophy in the entorhinal cortex and hippocampus. The second indicator was the extent of significant atrophy in the region of the whole brain, essentially the percentage of coordinates with a Z-score exceeding a threshold value (2.0) in the entire brain. We defined reproducibility as a coefficient of variation (CV) for these two indicators between the first and second scans.

III. RESULTS

III.A. Phantom studies

All phantom images were acquired with MRI scanners approved by the J-ADNI at 38 clinical sites. Polynomial functions were determined from phantom images acquired at week 0 and applied to other phantom images acquired by the same scanner 1 week later. The polynomial function was of third order along the A/P and R/L directions, and second order along the S/I direction. RMS errors of corrected phantom images obtained using a fourth- or fifth-order polynomial function vary less than RMS errors for the result obtained using a polynomial function of third order.

The resulting uncorrected images and images corrected using the J-ADNI, GW, and GW-plus-scaling correction methods are shown in Fig. 2. A red circle and yellow circle are superimposed on the outer and inner edges of the phantom shell, respectively. In the figure, although the outline of a phantom should be spherical, uncorrected and corrected GW phantom images are not circular. However, the outline of a corrected phantom image subject to the J-ADNI method appears to be circular. An example of the spatial distribution of fiducial sphere errors in a corresponding phantom image is shown in Fig. 3. Error levels corresponding to fiducial sphere positions are indicated by arrows of different color. A red arrow indicates errors over 3 mm, yellow indicates errors of 2–3 mm, blue indicates errors of 1–2 mm, and gray indicates errors of 0–1 mm. The direction of the arrow indicates the direction of the highest error at the orthogonal coordinate. Figures 3(b) and 3(c) show remaining errors over 1.0 mm at positions of designed fiducial spheres. However, the result of the J-ADNI method shows the errors of fiducial spheres under a voxel resolution of 1.0 mm. Therefore, the results show that our distortion correction method is qualitatively more efficient than other correction methods.

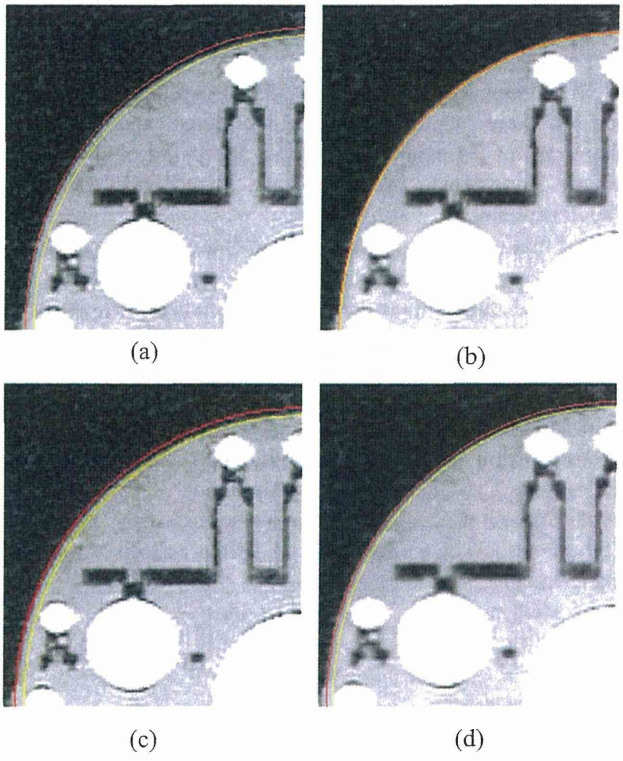

FIG. 2. Phantom across the axial plane. (a) Uncorrected; (b) corrected with the J-ADNI method; (c) GW correction; and (d) GW (nonlinear) and scaling correction (linear). The distance between the yellow and red circles shows the distortion level at the outer shell of the phantom.

For quantitative assessment of our method of correcting phantom images, we calculated the RMS error distribution. The distribution was obtained from uncorrected phantom images and phantom images corrected using Aqual2 and the CR. An incircle and circumcircle were manually drawn on the orthogonal plane of a phantom image (Fig. 4). The median RMS error was 0.615 mm for uncorrected phantom images and 0.257 mm for corrected images. The median CR was 0.985

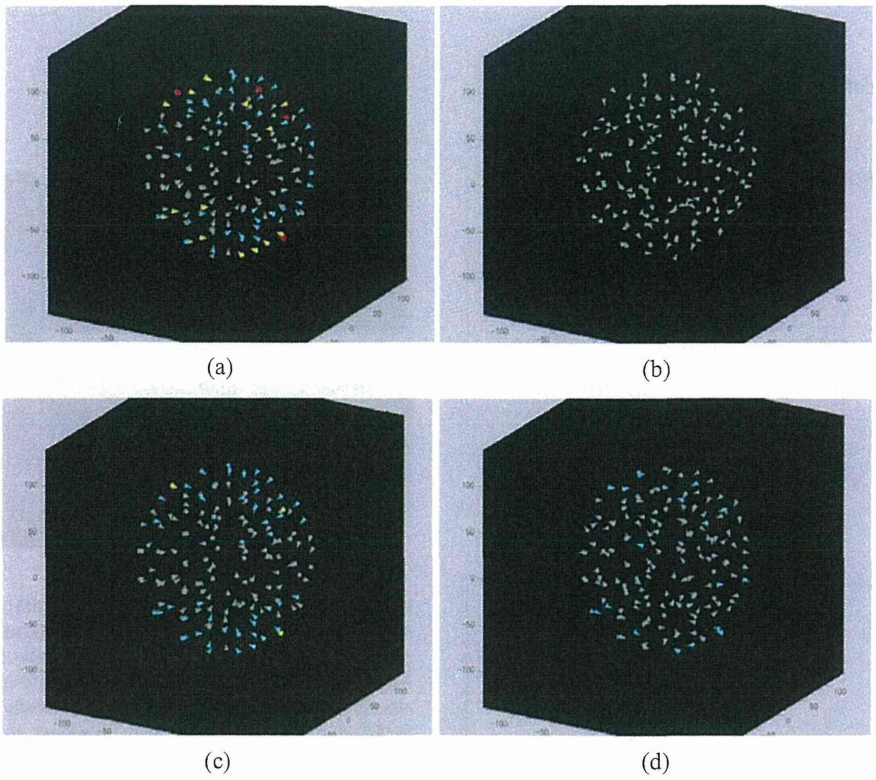

FIG. 3. Spatial distributions of fiducial sphere errors (differences) between obtained and designed coordinate values in phantom images. The arrows indicate the direction and magnitude of error. Colors indicate error levels at corresponding positions of fiducial spheres. The direction of an arrow corresponds to the basis vector with the highest magnitude of error. Red indicates error exceeding 3 mm; yellow indicates error of 2–3 mm; blue indicates error of 1–2 mm; and gray indicates error of 0–1 mm. (a) Uncorrected; (b) corrected with the J-ADNI method; (c) GW correction; and (d) GW and scaling correction.

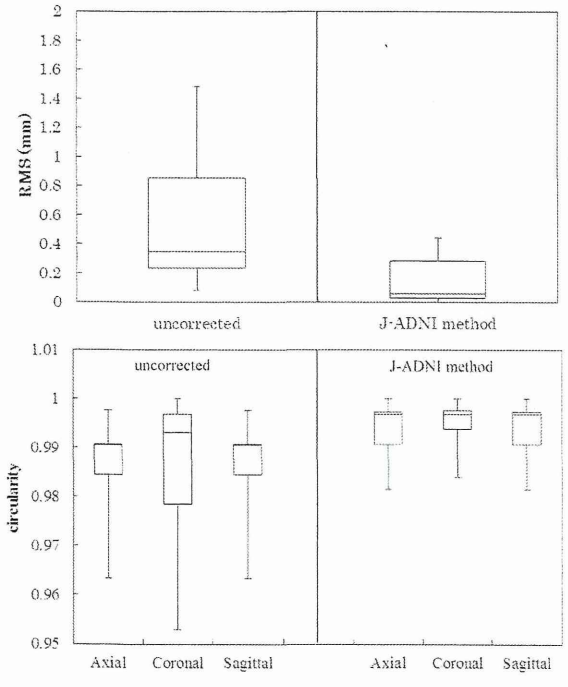

FIG. 4. RMS error and CR plots of uncorrected and corrected (J-ADNI method) phantom images ($N = 42$) obtained from all scanners for evaluation of effectiveness. (a) and (b) RMS errors obtained from analysis of phantom images by Aqual2. (c) and (d) CR plots for axial, coronal, and sagittal sections that were uncorrected (c) and corrected with the J-ADNI method (d).

for uncorrected axial images, 0.993 for uncorrected coronal images, and 0.991 for uncorrected sagittal images. After distortion correction, the median CR was 0.997 for axial images, 0.997 for coronal images, and 0.997 for sagittal images. RMS errors and the CR for all slices significantly improved (Wilcoxon signed-rank test, $p < 0.001$) after J-ADNI distortion correction.

These results show that the CR of a corrected image following application of the J-ADNI method was better than that of an uncorrected image for all slices. It is clear from Fig. 4 that the J-ADNI method improved RMS errors and the CR, and effectively corrected geometrical distortion in all phantom images.

To compare the performance of our method with that of GW correction and that of phantom-based scaling correction in addition to GW correction, we calculated RMS errors and the CR for phantom images as described previously. We obtained this information from GE Healthcare Japan and were therefore only able to apply GW correction to 11 images acquired by a group of GE scanners. The RMS errors in phase-encoding and slice-encoding directions, and CR results in the axial plane, both uncorrected and corrected with each method, are shown in Fig. 5. The top panel indicates that median RMS errors were 0.259 mm for uncorrected phantom images, 0.0976 mm for J-ADNI-corrected images, 0.268 mm for GW-corrected images, and 0.187 mm for GW-plus-scaling-corrected images along the phase-encoding direction.

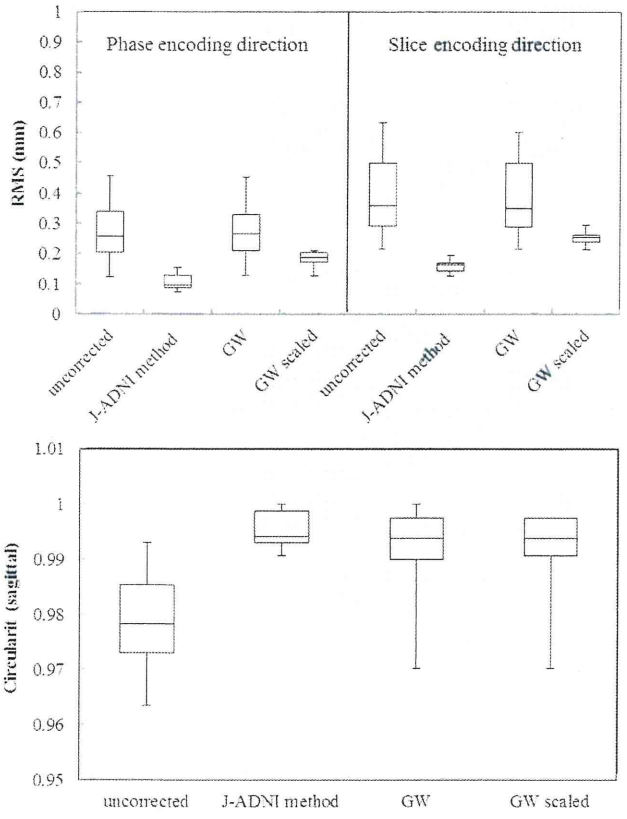

FIG. 5. RMS errors and CR plots ($N = 12$) for comparison of effectiveness of the J-ADNI, GW, and GW-plus-scaling correction methods for a confined group of GE scanners. The top panel shows RMS errors calculated by Aqual2 in the phase-encoding, A/P, direction (a) and slice-encoding, R/L, direction (b). The bottom panel shows CR plots for axial phantom images (c). These directions and (axial) plane suffered only the contribution of the gradient nonlinearity of distortion.

The corresponding values were 0.359 mm for uncorrected phantom images, 0.164 mm for J-ADNI-corrected images, 0.350 mm for GW-corrected images, and 0.255 mm for GW-plus-scaling-corrected images along the slice-encoding direction. The bottom panel shows the median CRs for the axial images: 0.978 for uncorrected images, 0.994 for J-ADNI-corrected images, 0.994 for GW-corrected images, and 0.994 for GW-plus-scaling-corrected images. The J-ADNI method improved RMS errors significantly compared with using uncorrected, GW, and GW-scaling correction methods along the phase-encoding direction and slice-encoding direction ($p < 0.001$).

CRs of the phantom image corrected with the J-ADNI method, GW, and GW-plus-scaling correction showed significant error reduction compared with the uncorrected image (Steel–Dwass test; $p < 0.001$, $p = 0.028$, and $p = 0.014$, respectively). However, there was almost no difference in the CR when comparing the J-ADNI method with the GW and GW-plus-scaling corrections despite there being CR differences for a specific image as shown in Fig. 2.

III.B. Reproducibility of VBM analysis

We performed Z-score analysis using automated VBM software. Ideally, CV for indicators in test–retest studies

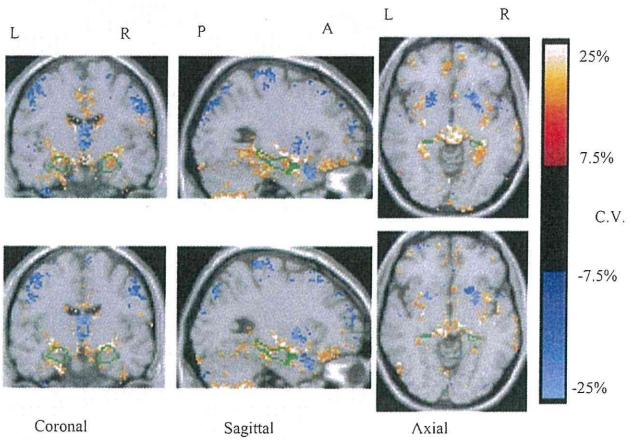

FIG. 6. Map of median CVs obtained by VBM Z-score analysis. Top and bottom rows show CV maps for an uncorrected image and a distortion-corrected image (J-ADNI method), respectively. The color-scaled CV map ranges from −25.0% to −7.5% and from 7.5% to 25.0% are displayed by overlaying orthogonal sections of the anatomically standardized MRI. Areas enclosed by green lines show medial temporal structures. Note the decrease in CV following distortion correction for the whole brain.

should be zero for a subject where there is no expectation of morphological changes associated with brain atrophy. CV maps drawn by comparing the initial and second Z-score analyses of uncorrected and corrected brain images of 38 healthy volunteers are shown in Fig. 6. The top and bottom rows show results for uncorrected and corrected brain images, respectively. In these maps, color voxels have a median value of 38 for the volunteer's CV of the Z-score between the first and second scans and the voxels are overlaid with orthogonal sections of the anatomically standardized MRI. The color scale range was −25.0% to −7.5% and 7.5% to 25.0%. Areas enclosed by green lines indicate medial temporal structures having the most significant decline of gray matter concentration at the very early stages of AD (Matsuda *et al.*[8]).

We obtained CVs of the averaged Z-score in the medial temporal structures. The extent of a region showing significant atrophy between first and second scans obtained using automated VBM software is shown in Fig. 7. The median CV of the averaged Z-score in the medial temporal structures after distortion correction using our method was 2.68%, which is not a significant improvement when comparing with uncorrected images. The median CV of the percentage of coordinates with a Z-score exceeding the threshold in the entire brain improved from 3.46% to 2.70% after distortion correction using the J-ADNI method (Wilcoxon signed-rank test, $p < 0.05$).

IV. DISCUSSION

To accurately measure the atrophy of brain structures such as the hippocampus, and to explore surrogate biomarkers obtained from MRI, geometrical distortion needs to be corrected. The US-ADNI uses two types of distortion correction methods: GW and phantom-based scaling correction. GW is only used to correct nonlinearities of geometrical distortion,

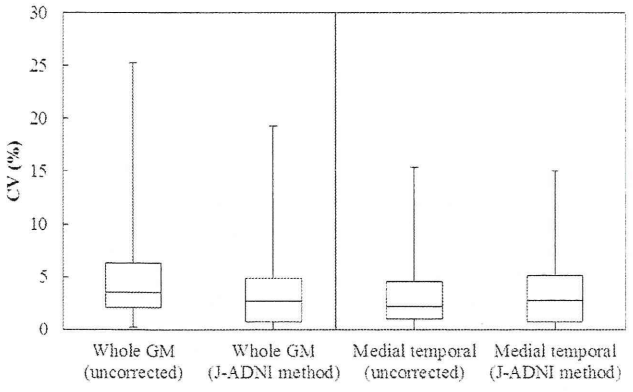

FIG. 7. CV between the baseline and second scan for uncorrected and corrected brain images ($N = 42$). The extent of atrophy variance in the whole-brain gray matter (GM) is shown (a), alongside the average Z-score for the medial temporal structures of the gray matter, which was determined using automated VBM software (b).

whereas scaling correction is used to correct linear scaling distortion.[19] According to Eq. (1), the first order of the polynomial function corresponds to the scaling factor of transformation and can correct linear scaling correction. Higher orders correct residual distortion; i.e., nonlinearities of distortion. Therefore, the J-ADNI method, which is based on a polynomial equation, can correct both nonlinear and linear geometrical distortions concurrently, and the method corresponds to phantom-based scaling correction and GW correction used by the US-ADNI.

Figure 4 shows that RMS errors and CRs in phantom studies significantly improved after J-ADNI distortion correction. In particular, RMS errors reduced by several millimeters to below the voxel resolution of 1.0 mm following application of the J-ADNI method. The structural analysis of brain images, such as voxel-based volume measurements within a region of interest, requires accuracy below the voxel resolution. Figure 4 shows that our method has enhanced reliability for volumetric brain image analysis.

We examined the ability of the J-ADNI, GW, and GW-plus-scaling correction methods to correct distortion arising from gradient nonlinearity. Figure 5 shows that RMS errors after GW correction did not change. This may be because of the efficiency limit of GW, as subsequent scaling correction reduced RMS errors significantly. These results show that the distortion arising from gradient nonlinearity includes a component that cannot be described by generic coil information and demonstrate the necessity of ADNI phantom-based scaling correction in addition to GW correction. In fact, the necessity of scaling correction through the registration of nine degrees of freedom has been reported.[19,27] Furthermore, GW corrects geometrical distortion according to the geometry of the generic gradient coil construction. If the gradient nonlinearity changes for the same scanner model, GW cannot correct this variability. Figure 5 shows that our method can reduce RMS errors more than GW and GW-plus-scaling correction. Hence, our method can describe distortion arising from gradient nonlinearity and correct it.

In contrast, the CR following implementation of the J-ADNI method was not statistically significant compared with the CRs following GW correction and GW-plus-scaling correction. The CR was obtained by drawing two circles on the border of the phantom outer shell and background, and its sensitivity was the pixel unit. Moreover, these circles were drawn manually and there were user-introduced errors at the level of the pixel unit. For the above reasons, the CR of the phantom image can be used to assess the adequacy of correction in the overall region, but may not be a good metric with which to correctly quantify and compare distortion correction methods.

However, the J-ADNI method detected fiducial sphere position errors and estimated geometrical distortion fields in phantom images for each scan, and corrected the nonlinearity and linearity of distortion. It was therefore used successfully to correct gradient variability.

The J-ADNI method demonstrates improved RMS error assessment and can thus correct geometrical distortion, thereby improving the reliability and accuracy of volumetric and/or morphometric analysis of structural MRI brain images.

In human studies, the reproducibility of VBM analysis for whole-brain gray matter was significantly improved after distortion correction using the J-ADNI method. We assumed that the CR of the outer shell of the phantom affects the measurement accuracy of the broad structure volume, which is necessary for whole-brain imaging. The CR was improved using either the J-ADNI or GW method, corresponding to improved accuracy in describing the broad structure. Geometrical distortion resulted in apparent volume changes and partial volume effects at each voxel. Our method corrected these erroneous volume changes and partial volume effects through image warping and mass-preservation resampling, respectively. Repeatability of subsequent analyses was improved after distortion correction. However, the reproducibility of VBM analysis for medial temporal structures was not significantly improved using our method because fiducial position error was more common in the outer region of the phantom image, as shown in Fig. 2. In fact, medial temporal structures originally showed low variation in VBM analysis (Fig. 6). Therefore, effects of distortion correction may be smaller than those observed for the whole brain. Alternatively, the efficacy of distortion correction is seen for the whole-brain gray matter including the region of large distortion. Our future task is to investigate the performance of our method for anatomical structures around the surface of the brain that are expected to suffer from distortion in human studies; e.g., the cortical thickness, lateral temporal lobe, and inferior parietal lobe.

The GW method requires information about the gradient coil, which can only be provided by the manufacturer, and the method can only be applied to MRI scanners produced by GE and Siemens. Our method requires scanning of a phantom image to correct geometric distortion of a subject's brain image and can be adapted to all scanners. The ADNI phantom is commercially available and can be easily purchased. However, the phantom-based correction method requires additional scanning to obtain a phantom image for correction.

A multisite study such as the ADNI can monitor scanner performance by scanning the ADNI phantom. Our method uses this scan, and we can thus correct distortion by making one phantom scan serve a dual purpose.

In future studies, we will investigate the period of validity for the distortion field obtained from a phantom image. This would assist in reducing the cost of conducting a phantom scan. We also intend to propose an optimal phantom scanning design for distortion correction using our developed method associated with scanner performance monitoring.

ACKNOWLEDGMENTS

This study is part of the "Translational Research Promotion Project/Research project for the Development of a Systematic Method for the Assessment of Alzheimer's Disease," sponsored by the New Energy and Industrial Technology Development Organization (NEDO) of Japan. The J-ADNI is also supported by a Grant-in-Aid for Comprehensive Research on Dementia from the Japanese Ministry of Health, Labour, and Welfare, as well as by grants from J-ADNI Pharmaceutical Industry Scientific Advisory Board (ISAB) companies. The authors would like to thank the J-ADNI Imaging ISAB and other organizations for their support of this work.

[a]Author to whom correspondence should be addressed. Electronic mail: maikusa@ncnp.go.jp

[1]C. Fennema-Notestine, D. J. Hagler, Jr., L. K. McEvoy, A. S. Fleisher, E. H. Wu, D. S. Karow, A. M. Dale, and Alzheimer's Disease Neuroimaging Initiative, "Structural MRI biomarkers for preclinical and mild Alzheimer's disease," Hum. Brain. Mapp. **30**(10), 3238–3253 (2009).

[2]B. C. Dickerson, I. Goncharova, M. P. Sullivan, C. Forchetti, R. S. Wilson, D. A. Bennett, L. A. Beckett, and L. deToledo-Morrell, "MRI-derived entorhinal and hippocampal atrophy in incipient and very mild Alzheimer's disease," Neurobiol. Aging **22**, 747–754 (2001).

[3]D. Holland, J. B. Brewer, D. J. Hagler, C. Fennema-Notestine, A. M. Dale, and Alzheimer's Disease Neuroimaging Initiative, "Subregional neuroanatomical change as a biomarker for Alzheimer's disease," Proc. Natl. Acad. Sci. U.S.A. **106**(49), 20954–20959 (2009).

[4]M. Grundman, D. Sencakova, C. R. Jack, Jr., R. C. Petersen, H. T. Kim, A. Schultz, M. F. Weiner, C. DeCarli, S. T. DeKosky, C. Dyck, R. G. Thomas, and L. J. Thal, "Alzheimer's disease cooperative study brain MRI hippocampal volume and prediction of clinical status in a mild cognitive impairment trial," J. Mol. Neurosci. **19**, 23–27 (2002).

[5]C. R. Jack, Jr., R. C. Petersen, Y. C. Xu, S. C. Waring, P. C. O'Brien, E. G. Tangalos, G. E. Smith, R. J. Ivnik, and E. Kokmen, "Medial temporal atrophy on MRI in normal aging and very mild Alzheimer's disease," Neurology. **49**, 786–794 (1997).

[6]S. Klöppel, C. M. Stonnington, C. Chu, B. Draganski, R. I. Scahill, J. D. Rohrer, N. C. Fox, C. R. Jack, Jr., J. Ashburner, and R. S. J. Frackowiak, "Automatic classification of MR scans in Alzheimer's disease," Brain **131**, 681–689 (2008).

[7]B. Magnin, L. Mesrob, S. Kinkingnéhun, M. Pélégrini-Issac, O. Colliot, M. Sarazin, B. Dubois, S. Lehéricy, and H. Benali, "Support vector machine-based classification of Alzheimer's disease from whole-brain anatomical MRI," Neuroradiology **51**, 73–83 (2009).

[8]H. Matsuda, S. Mizumura, K. Nemoto, F. Yamashita, E. Imabayashi, N. Sato, and T. Asada, "Automatic voxel-based morphometry of structural MRI by SPM8 plus diffeomorphic anatomic registration through exponentiated Lie algebra improves the diagnosis of probable Alzheimer disease," AJNR Am. J. Neuroradiol. **33**, 1109–1114 (2012).

[9]P. Vemuri, J. L. Gunter, M. L. Senjem, J. L. Whitwell, K. Kantarci, D. S. Knopman, B. F. Boeve, R. C. Petersen, and C. R. Jack, Jr., "Alzheimer's disease diagnosis in individual subjects using structural MR images: Validation studies," Neuroimage **39**, 1186–1197 (2008).

[10]B. Dubois, H. H. Feldman, C. Jacova, S. T. Dekosky, P. Barberger-Gateau, J. Cummings, A. Delacourte, D. Galasko, S. Gauthier, G. Jicha, K. Meguro, J. O'brien, F. Pasquier, P. Robert, M. Rossor, S. Salloway, Y. Stern, P. J. Visser, and P. Scheltens, "Research criteria for the diagnosis of Alzheimer's disease: Revising the NINCDS-ADRDA criteria," Lancet Neurol. **6**(8), 734–746 (2007).

[11]R. Cuingnet, E. Gerardin, J. Tessieras, G. Auzias, S. Lehéricy, M. O. Habert, M. Chupin, H. Benali, and O. Colliot, "Automatic classification of patients with Alzheimer's disease from structural MRI: A comparison of ten methods using the ADNI database," Neuroimage **56**, 766–781 (2011).

[12]S. K. Madsen, A. J. Ho, X. Hua, P. S. Saharan, A. W. Toga, C. R. Jack, Jr., M. W. Weiner, and P. M. Thompson, "3D maps localize caudate nucleus atrophy in 400 Alzheimer's disease, mild cognitive impairment, and healthy elderly subjects," Neurobiol. Aging **31**, 1312–1325 (2010).

[13]C. R. Jack, Jr., M. A. Bernstein, N. C. Fox, P. Thompson, G. Alexander, D. Harvey, B. Borowski, P. J. Britson, J. L. Whitwell, C. Ward, A. M. Dale, J. P. Felmlee, J. L. Gunter, D. L. Hill, R. Killiany, N. Schuff, S. Fox-Bosetti, C. Lin, C. Studholme, C. S. DeCarli, G. Krueger, H. A. Ward, G. J. Metzger, K. T. Scott, R. Mallozzi, D. Blezek, J. Levy, J. P. Debbins, A. S. Fleisher, M. Albert, R. Green, G. Bartzokis, G. Glover, J. Mugler, and M. W. Weiner, "The Alzheimer's Disease Neuroimaging Initiative (ADNI): MRI methods," J. Magn. Reson. Imaging **27**(4), 685–691 (2008).

[14]T. Iwatsubo, "Japanese Alzheimer's Disease Neuroimaging Initiative: Present status and future," Alzheimers Dement. **6**, 297–299 (2010).

[15]A. Janke, H. Zhao, G. J. Gowin, G. J. Galloway, and D. M. Doddrell, "Use of spherical harmonic deconvolution methods to compensate for nonlinear gradient effects on MRI images," Magnet. Reson. Med. **52**, 115–122 (2004).

[16]Z. Caramanos, V. S. Fonov, S. J. Francis, S. Narayanan, G. B. Pike, D. L. Collins, and D. L. Arnold, "Gradient distortions in MRI: Characterizing and correcting for their effects on SENA-generated measures of brain volume change," Neuroimage **49**, 1601–1611 (2010).

[17]L. N. Baldwin, K. Wachowicz, and S. D. Thomas, "Characterization, prediction and correction of geometric distortion in 3 T MRI images," Med. Phys. **34**, 388–399 (2007).

[18]A. D. Leow, A. D. Klunder, C. R. Jack, Jr., A. W. Toga, A. M. Dale, M. A. Bernstein, P. J. Britson, J. L. Gunter, C. P. Ward, J. L. Whitwell, B. J. Borowski, A. S. Fleisher, N. C. Fox, D. Harvey, J. Kornak, N. Schuff, C. Studholme, G. E. Alexander, M. W. Weiner, P. M. Thompson, and ADNI Preparatory Phase Study, "Longitudinal stability of MRI for mapping brain change using tensor-based morphometry," Neuroimage **31**, 627–640 (2006).

[19]J. L. Gunter, M. A. Bernstein, B. J. Borowski, C. P. Ward, P. J. Britson, and J. P. Felmlee, "Measurement of MRI scanner performance with the ADNI phantom," Med. Phys. **36**, 2193–2205 (2009).

[20]L. Schad, S. Lott, F. Schmitt, V. Sturm, and W. J. Lorenz, "Correction of spatial distortion in MRI image: A prerequisite for accurate stereotaxy," J. Comput. Assist. Tomogr. **11**, 499–505 (1987).

[21]S. Langlois, M. Desvigness, J. M. Constans, and M. Revenu, "MRI geometric distortion: A simple approach to correcting the effects of non-linear gradient fields," J. Comput. Assist. Tomogr. **9**, 821–831 (1999).

[22]C. Menuel, L. Garnero, E. Bardinet, F. Poupon, D. Phalippou, and D. Dormont, "Characterization and correction of distortions in stereotactic magnetic resonance imaging for bilateral subthalamic stimulation in Parkinson disease," J. Neurosurg. **103**, 256–266 (2005).

[23]A. R. Liddle, "Information criteria for astrophysical model selection," Mon. Not. Roy. Astron. Soc. Lett. **377**, L74-L78 (2007).

[24]G. Schwarz, "Estimating the dimension of a model," Ann. Stat. **6**, 461–464 (1978).

[25]J. Jovicich, S. Czanner, D. Greve, E. Haley, A. van der Kouwe, R. Gollub, D. Kennedy, F. Schmitt, G. Brown, J. MacFall, B. Fischl, and A. Dale, "Reliability in multi-site structural MRI studies: Effects of gradient non-linearity correction on phantom and human data," Neuroimage **30**, 436–443 (2006).

[26]C. J. C. Bakker, M. A. Moerland, R. Bhagwandien, and R. Beersma, "Analysis of machine-dependent and object-induced geometric distortion if 2DFT MR imaging," Magn. Reson. Imaging **10**, 597–608 (1992).

[27]M. J. Clarkson, S. Ourselin, C. Nielsen, K. K. Leung, J. Barnes, J. L. Whitwell, J. L. Gunter, D. L. Hill, M. W. Weiner, C. R. Jack, Jr., N. C. Fox, and Alzheimer's Disease Neuroimaging Initiative, "Comparison of phantom and registration scaling corrections using the ADNI cohort," Neuroimage **47**, 1506–1513 (2009).

Brain and Behavior

Open Access

Comparison between brain CT and MRI for voxel-based morphometry of Alzheimer's disease

Etsuko Imabayashi[1,2], Hiroshi Matsuda[3], Takeshi Tabira[4], Kunimasa Arima[5], Nobuo Araki[6], Kenji Ishii[7], Fumio Yamashita[8], Takeshi Iwatsubo[9] & Japanese Alzheimer's Disease Neuroimaging Initiative

[1]Department of Radiology, Tokyo Metropolitan Geriatric Hospital and Institute of Gerontology, 35-2 Sakaecho, Itabashi-ku, Tokyo, Japan
[2]Department of Nuclear Medicine, Saitama Medical University International Medical Center, Saitama, Japan
[3]Integrative Brain Imaging Center, National Center of Neurology and Psychiatry, Tokyo, Japan
[4]Department of Diagnosis, Prevention and Treatment of Dementia, Graduate School of Medicine, Juntendo University, Tokyo, Japan
[5]Department of Psychiatry, National Center Hospital, National Center of Neurology and Psychiatry, Tokyo, Japan
[6]Department of Neurology, Saitama Medical University Hospital, Saitama, Japan
[7]Department of Positron Medical Center, Tokyo Metropolitan Institute of Gerontology, Tokyo, Japan
[8]Division of Ultrahigh Field MRI, Core of Multidisciplinary Research for Medical Imaging, Institute for Biomedical Sciences of Iwate Medical University, Iwate, Japan
[9]Department of Neuropathology and Neuroscience, Graduate School of Pharmaceutical Sciences, University of Tokyo, Tokyo, Japan

Keywords
Alzheimer's disease, CT, PIB, VBM

Correspondence
Etsuko Imabayashi, Department of Radiology, Tokyo Metropolitan Geriatric Hospital and Institute of Gerontology, 35-2 Sakaecho, Itabashi-ku, Tokyo, Japan.
Tel: +81-3-3964-1141; Fax: +81-3-3964-1148; E-mail: mbysh@hotmail.com

Funding Information
No funding information is provided.

Received: 7 February 2013; Revised: 30 April 2013; Accepted: 6 May 2013

Brain and Behavior **2013; 3(4): 487–493**

doi: 10.1002/brb3.146

Abstract

The voxel-based morphometry (VBM) technique using brain magnetic resonance imaging (MRI) objectively maps gray matter loss on a voxel-by-voxel basis after anatomic standardization. In patients with Alzheimer's disease (AD), reductions of gray matter volume, mainly in the medial temporal structures, have been reported; however, inhomogeneity and geometric distortion of the field intensity hampers the reproducibility of MRI. In the present study, we developed a novel computed tomography (CT)-based VBM method and used this technique to detect volume loss in AD patients as compared with normal controls. The results were compared with MRI-based VBM using the same subjects. Pittsburgh Compound B (^{11}C-PIB) positron emission tomography (PET)/CT was performed and two experts in neuro-nuclear medicine judged whether regional amyloid β load was consistent with a diagnosis of AD. Before the injection of ^{11}C-PIB, high-quality CT scans were obtained using the same PET/CT equipment. MRI was performed within a mean interval of 25.1 $\pm$ 8.2 days before the PET/CT scan. Using statistical parametric mapping 8 (SPM8), the extracted gray matter images from CT and MRI were spatially normalized using a gray matter template and smoothed using a Gaussian kernel. Group comparisons were performed using SPM8 between five ^{11}C-PIB-positive patients with probable AD and seven ^{11}C-PIB-negative age-matched controls with normal cognition. Gray matter volumes in the bilateral medial temporal areas were reduced in the AD group as compared with the cognitively normal group in both CT-based VBM (in the left; $P < 0.0001$, cluster size 2776 and in the right; $P < 0.0001$, cluster size 630) and MRI-based VBM (in the left; $P < 0.0001$, cluster size 381 and in the right, $P < 0.0001$, cluster size 421). This newly developed CT-based VBM technique can detect significant atrophy in the entorhinal cortex in probable AD patients as previously reported using MRI-based VBM. However, CT-VBM was more sensitive and revealed larger areas of significant atrophy than MR-VBM.

Introduction

Macroscopically, the brain has a simple structure, despite its complex functions. Morphologically, brain structures consist mainly of gyri and sulci, with these structures being quite common in human beings. This simplicity makes it easier to normalize the brain to an anatomically standardized space and to introduce voxel-based statistical

analysis. Histologically, the majority of brain tissue consists of gray matter, white matter, and cerebrospinal fluid space. Gray matter thickness reflects the number of residual neurons. Commonly, brain magnetic resonance imaging (MRI) has been used to derive anatomical and tissue volume information, especially in gray and white matter.

The voxel-based morphometry (VBM) technique objectively maps gray matter loss on a voxel-by-voxel basis after anatomic standardization. This is one of the simplest methods available to avoid subjectivity and dependence on an a priori hypothesis and to adopt the principle of data-driven analysis (Ashburner and Friston 2000). In patients with Alzheimer's disease (AD), a significant reduction of gray matter volume in the hippocampal formation and entorhinal cortex has been described (Ohnishi et al. 2001; Hirata et al. 2005). For the voxel-wise comparison of gray matter between two groups of subjects, MRI has been used as a matter of course.

In the present study, we developed a novel computed tomography (CT)-based VBM (CT-VBM) technique. Brain CT has more homogeneity and much less distortion than MRI, even when using different machines or scan protocols. It is also relatively economical and widely available. Moreover, nowadays, CT data are easily available from a routine positron emission tomography (PET)/CT study. In the present study, we also compared the results from CT-VBM with those from MRI-based VBM (MR-VBM) using the same individuals.

Materials and Methods

Subjects

All of the subjects were enrolled in the Japanese Alzheimer's Disease Neuroimaging Initiative (J-ADNI). The J-ADNI study was approved by the ethics committee of our institution. All study subjects gave written informed consent prior to participation.

Five AD patients (three females and two males, 73.8 ± 20.7 years old) and 7 age-matched cognitively normal controls (three females and four males, 70.1 ± 9.81 years old) were assessed in this study. The patients were diagnosed with AD when they fulfilled the DSM-IV criteria for dementia and the revised National Institute of Neurologic and Communicative Disorders and Stroke-AD and Related Disorders Association criteria (Dubois et al. 2010) for probable AD and registered with the J-ADNI study as AD patients.

All of the AD patients showed positive Pittsburgh Compound B (^{11}C-PIB) accumulation and all of the cognitively normal controls showed no ^{11}C-PIB accumulation.

PET/CT

^{11}C-PIB-PET/CT was performed in all subjects in the Department of Nuclear Medicine of Saitama Medical University International Medical Center. Each subject received an intravenous injection of 600 MBq of *N*-methyl-[^{11}C] 2-(4′-methylamino-phenyl)-6-hydroxybenzothiazole (^{11}C-PIB) (Klunk et al. 2004) and underwent a 70 min list mode acquisition using PET/CT equipment with high spatial resolution (Biograph 6 Hi-Rez; Siemens Medical Solutions USA, Inc., Knoxville, TN). The combination of Fourier rebinning and ordered subsets expectation maximization with an iteration number of four, subset of 16, and an all-pass filter were used for PET image reconstruction and framing into 25 volumes: 10 sec × 6, 20 sec × 3, 60 sec × 2, 180 sec × 2, and 300 sec × 12. Attenuation correction was performed using the CT data.

Before the intravenous injection of ^{11}C-PIB, high quality CT scans were obtained using the same PET/CT equipment. The scanning parameters were held constant in the helical scanning mode: 1.0-sec gantry rotation time, 130 kVp, 150–240 mAsec, 0.5:1 beam pitch, 3-mm table feed per gantry rotation, and 6 × 2 mm detector configuration. The images were reconstructed at 3-mm thickness with filtered back projection, a display field of view of 25 cm, and a reconstruction matrix size of 512 × 512.

MRI

MRI scans were also performed in all subjects within a mean interval of 25.1 ± 8.2 days (14–40 days) before the PET/CT scan. The scans were acquired on a 1.5 T scanner using a three-dimensional (3D) sagittal magnetization-prepared rapid gradient-echo imaging sequence, which was specially adjusted for the US-ADNI protocols (http://adni.loni.ucla.edu/research/protocols/mri-protocols/). Repetition time (TR), echo time (TE), inversion time (TI), and flip angle were 9.2 msec, 40 msec, 225 msec, and 8°, respectively. The in-plane resolution was 256 × 256 (1.25 × 1.25 mm) with a slice thickness of 1.2 mm.

Image analysis of ^{11}C-PIB PET

Data analyses of ^{11}C-PIB PET were performed using the PMOD software package (version 3.0; PMOD Technologies, Ltd., Zürich, Switzerland). Distribution volume ratio images referenced to the cerebellum were generated using noninvasive Logan graphical analysis (Price et al. 2005). Two experts in neuro-nuclear medicine, both with over 10 years of experience, interpreted the regional β amyloid load, focusing on whether it was consistent with a diagnosis of AD.

Gray matter extraction from brain MRI

In statistical parametric mapping 8 (SPM8) (http://www.fil.ion.ucl.ac.uk/spm), we use the default segmentation parameters for MR images because this program is originally developed for MRI images; with very light regularization, warp frequency cut-off of 25 Hz, a shorter sampling distance of 3, and a customized number of Gaussians per tissue class for each patient: 2 for gray and white matter, 2 for cerebrospinal fluid, and 4 for other tissues. The MR images were then segmented to gray matter, white matter, cerebrospinal fluid, and other compartments using an unmodified version of the clustering algorithm (Ashburner and Friston 2000).

Gray matter extraction from brain CT

We changed many default setting to the segmentation program in SPM8 taking the difference of CT and MR into account. Before using the segmentation function in SPM8, MRIcro (http://www.cabiatl.com/mricro) and Image J (http://rsb.info.nih.gov/ij) were used to preprocess the CT images. The Brain Extraction Tool (Smith 2000) in MRIcro was used to remove the head holder segment. Image J was used to make the bounding box and voxel sizes equivalent to the tissue probability maps in SPM8. In SPM8, we set the segmentation parameters with extremely heavy regularization for unbiased CT images, a larger warp frequency cut-off of 35 Hz, a shorter sampling distance of 2, and a customized number of Gaussians per tissue class for each patients: 1 or 2 for gray and white matter and 6–8 for cerebrospinal fluid and other tissues. The number of Gaussians per tissue class was adjusted for each patient until successful segmentation was achieved. The CT images were then segmented to gray matter, white matter, cerebrospinal fluid, and other compartments using an unmodified version of the clustering algorithm (Ashburner and Friston 2000) (Fig. 1).

VBM

Segmented gray matter images, from both CT and MRI, for each original individual brain space were spatially normalized to a standard brain template (Talairach and Tournoux 1988) in a 3D space. Spatial normalization corrects for differences in brain size and shape and facilitates intersubject averaging. At the same time, voxel was modified to the same size: 2 mm × 2 mm × 2 mm. A priori gray matter images in SPM8 were used as a standard template. The gray matter images were then smoothed with a 12-mm, full-width half-maximum isotropic Gaussian kernel to use the partial volume effect to create a spectrum of gray matter intensities. The gray matter densities are equivalent to the weighted average of gray voxels located in the volume fixed by the smoothing kernel; therefore, regional intensities can be taken as being equivalent to gray matter volumes (Ashburner and Friston 2000; Ohnishi et al. 2001).

Statistical analysis

The processed images were analyzed using SPM8, which implements the general linear model. Global gray matter in the images was treated as a nuisance confounder. Proportional scaling was used to achieve global normalization

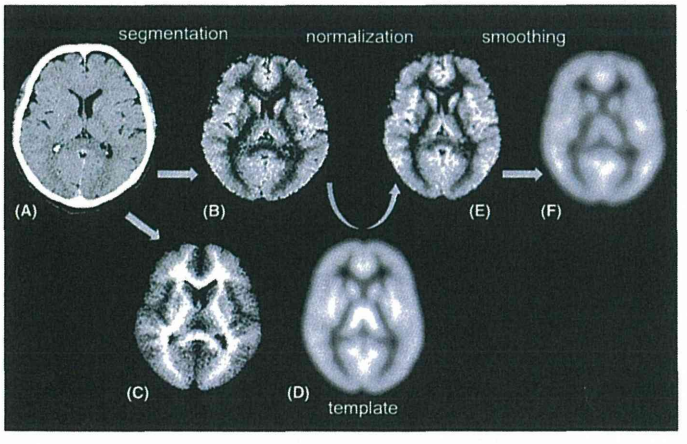

Figure 1. CT-based VBM procedure. (A) A slice from an original CT image. (B) Gray matter extracted from (A) using the segmentation module in SPM8. (C) White matter extracted from (B). (D) A priori template of gray matter in SPM8. (E) Spatially normalized gray matter image using (D). (F) Image smoothed to the Gaussian distribution. CT, computed tomography; VBM, voxel-based morphometry; SPM8, statistical parametric mapping 8.

of voxel values between the images. In the analysis of patients with AD, we studied the differences in the gray matter between the cognitively normal controls versus AD patients using t statistics. The resulting sets of t values constituted statistical parametric maps: SPM (t), which were transformed to the unit normal distribution (SPM [Z]). Group analysis of gray matter volume between the AD patients and cognitively normal controls was performed using a spatial extent threshold of 123 (984 mm^3) for CT-VBM and 381 (3048 mm^3) for MRI-VBM contiguous voxels. Main effects used whole-brain analyses with a threshold at a voxel level of $P < 0.005$ and a cluster false discovery rate of $P < 0.05$ for the multiple comparison correction (Chumbley and Friston 2009).

Results

In CT-VBM, the AD group showed a significant decrease of gray matter volume in the bilateral entorhinal cortex at Brodmann area (BA) 28, left hippocampus, in the left anterior cingulate gyri at BA 32, in the right temporopolar area, and in the right caudal head as compared to the cognitively normal group (Table 1 and Fig. 2).

In MR-VBM, the AD group showed a significant decrease of gray matter volume in the bilateral hippocampus and left entorhinal cortex at BA28 as compared with the cognitively normal group (Table 2 and Fig. 3). The most significant atrophy was observed in the left hippocampus.

Discussion

In AD patients, both CT-VBM and MR-VBM demonstrated significant atrophy in the left entorhinal cortex and hippocampus and in the right entorhinal cortex or hippocampus with left-side dominancy. Our hypothesis was that, even with the gray matter segmented from CT and not from MRI, the characteristic medial temporal lobe atrophy of AD patients can be detected using the VBM procedure. This hypothesis was proved in this study.

Numerous structural MRI studies have demonstrated that atrophy of the medial temporal lobe, including the hippocampus and entorhinal cortex, is a sensitive marker of early AD (Killiany et al. 2000; Du et al. 2001). Both the entorhinal cortex and hippocampus are essential parts of the medial temporal lobe system that supports declarative memory. Neuronal loss in AD is thought to start in the entorhinal cortex and spread to other regions, such as the hippocampus (Braak and Braak 1991). Guo et al. (2010) observed gray matter volume in 13 AD patients and 14 healthy controls using MRI. In their analysis of gray matter volume, the left parahippocampal gyrus showed more significant atrophy than the right. Shi et al. (2009) found left-less-than-right asymmetry patterns by comparing hippocampal volume. These investigations seem to be in good agreement with the present results of left-side dominant atrophy.

As a result, the gray matter atrophy in AD patients observed using CT-VBM was found to be more widespread than that observed using MR-VBM. Atrophy in the right caudate head, left anterior cingulate, and right temporal pole was only observed using CT-VBM in this study. In contrast to its precise spatial and tissue resolution, MRI shows deterioration in field intensity inhomogeneity and geometric distortion depending on factors such as the machines and sequences used and the position of the brain in the coil. Because this intensity inhomogeneity affects many automatic quantitative image analyses, various algorithms for correction have been introduced (Sled et al. 1998; Arnold et al. 2001). On the contrary, brain CT has more homogeneity and much less distortion than MRI, even when using different machines or scan protocols. This increased homogeneity and reduced distortion may result in more sensitivity. There is another possibility that the segmentation parameter could contribute to the difference of CT and MR to a certain extent. This new method should be confirmed with more subjects and diagnostic accuracy should be measured.

Atrophy in the temporal pole and anterior cingulate have been reported by MRI-based VBM (Karas et al.

Table 1. Results of CT-VBM.

	Brodmann area	Cluster size, voxels	Peak P (uncorrected)	Peak t value	Peak Z value	Talairach coordinate (x, y, z)		
L entorhinal cortex	28	2776	0.00000216	8.955	4.595	−24	3	−24
R caudate head			0.00000351	8.483	4.493	10	12	−1
L hippocampus			0.00000435	8.279	4.447	−34	−17	−19
L anterior cingulate	32	366	0.00000668	7.885	4.354	−2	34	17
R entorhinal cortex	28	630	0.00000281	6.664	4.029	30	−7	−25
R temporopolar area	38		0.00000292	6.632	4.019	32	7	−24

Locations of gray matter volume reductions in AD patients compared with cognitively normal controls. CT-VBM, computed tomography-based voxel-based morphometry; AD, Alzheimer's disease.

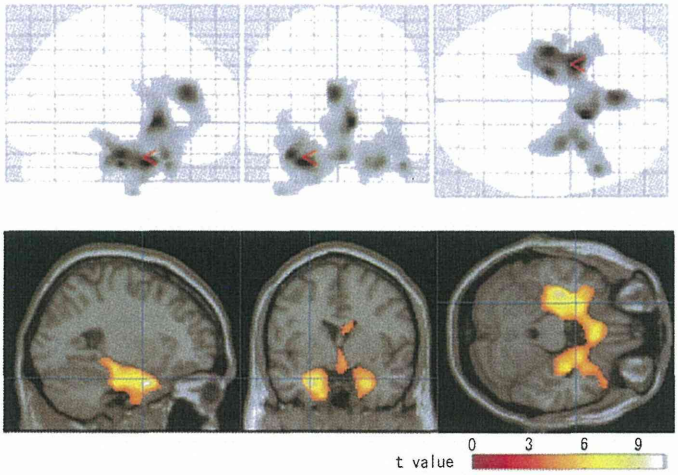

Figure 2. Significant reduction of regional gray matter volume is noted in the bilateral medial temporal cortex, temporopolar areas, right caudate, and anterior cingulate in AD patients with CT-VBM. Upper row: The SPM of the t statistics is displayed in a standard format as a maximum intensity projection viewed from the right hand side (left image), the back (middle image), and the top (right image) of the brain. The anatomic space corresponds to the atlas of Talairach and Tournoux. Lower row: Significance maps of decreased gray matter volume in AD patients superimposed on a T1-weighted brain MRI template image in Montreal Neurological Institute (MNI) space. The color bar represents the *t* value. AD, Alzheimer's disease; CT, computed tomography; VBM, voxel-based morphometry; SPM, statistical parametric mapping; MRI, magnetic resonance imaging.

Table 2. Results of MR-VBM.

	Brodmann area	Cluster size, voxels	Peak *P* (uncorrected)	Peak *t* value	Peak *Z* value	Talairach coordinate (*x*, *y*, *z*)		
L hippocampus		381	0.00000145	9.359	4.677	−30	−18	−13
L entorhinal cortex	28		0.0000636	6.028	3.832	−16	−14	−18
R hippocampus		421	0.0000024	8.854	4.574	30	−12	−16
R hippocampus			0.0000291	8.663	4.533	34	−20	−11

Locations of gray matter volume reductions in AD patients compared with cognitively normal controls. MR-VBM, magnetic resonance-based voxel-based morphometry; AD, Alzheimer's disease.

2003; Guo et al. 2010). These areas are also known to be pathologically involved in AD, where both amyloid deposition and neurofibrillary changes are observed (Braak and Braak 1991). The caudate head is known as a site at which amyloid and tau deposits also accumulate (Braak and Braak 1991). Madsen et al. (2010) showed a reduction of caudate volume in patients with mild cognitive impairment (MCI) and a further reduction in AD patients. They also showed a greater volume of the right caudate than the left caudate in cognitively normal controls and MCI subjects and twofold greater atrophy in the right caudate than in the left caudate in AD patients. They suggested that a possible confounding factor in some VBM studies of the caudate could result in the misregistration of anatomy across subjects along the ventricles. From our results, it was suggested that some artificial factors like cerebrospinal fluid flow may generate a confounding factor in MR-VBM; however, these are not detected on CT images.

Conclusion

The present study modified a conventional VBM procedure using brain CT instead of MRI to detect significant atrophy in AD patients. This CT-VBM technique revealed larger areas of significant atrophy than MR-VBM. CT-VBM revealed additional significant atrophy in the anterior cingulate and right caudate head to the medial

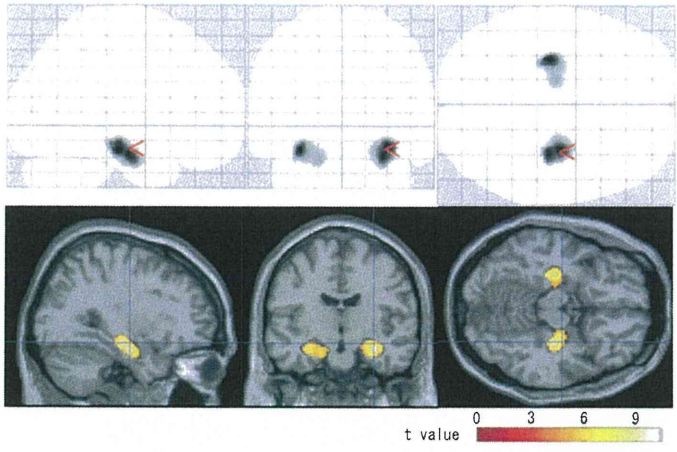

Figure 3. Significant reduction of regional gray matter volume is noted in the bilateral medial temporal cortex in AD patients with MR-VBM. Upper row: The SPM of the *t* statistics is displayed in a standard format as a maximum intensity projection viewed from the right hand side (left image), the back (middle image), and the top (right image) of the brain. The anatomic space corresponds to the atlas of Talairach and Tournoux. Lower row: Significance maps of decreased gray matter volume in AD patients superimposed on a T1-weighted brain MRI template image in Montreal Neurological Institute (MNI) space. The color bar represents the *t* value. AD, Alzheimer's disease; MR-VBM, magnetic resonance based voxel-based morphometry; SPM, statistical parametric mapping; MRI, magnetic resonance imaging.

temporal areas, which were only detected in a limited manner on MR-VBM.

At the present time, though, complementary use of CT-VBM and MR-VBM is desirable, and for clinical use, a simpler and proper program for CT-VBM or an advanced scanning technique for more precise tissue contrast without heavier radiation exposure would be desirable, our results suggest that CT-VBM has the potential to replace MR-VBM for diagnosing AD.

Acknowledgments

We are grateful to the radiology technicians of the Department of Nuclear Medicine of Saitama Medical University International Medical Center and of the Department of Radiology of Saitama Medical University Hospital for their technical support.

Conflict of Interest

None declared.

References

Arnold, J. B., J. S. Liow, K. A. Schaper, J. J. Stern, J. G. Sled, D. W. Shattuck, et al. 2001. Qualitative and quantitative evaluation of six algorithms for correcting intensity nonuniformity effects. Neuroimage 13:931–943.

Ashburner, J., and K. J. Friston. 2000. Voxel-based morphometry-the methods. Neuroimage 11:805–821.

Braak, H., and E. Braak. 1991. Neuropathological stageing of Alzheimer-related changes. Acta Neuropathol. 82:239–259.

Chumbley, J. R., and K. J. Friston. 2009. False discovery rate revisited: FDR and topological inference using Gaussian random fields. Neuroimage 44:62–70.

Du, A. T., N. Schuff, D. Amend, M. P. Laakso, Y. Y. Hsu, W. J. Jagust, et al. 2001. Magnetic resonance imaging of the entorhinal cortex and hippocampus in mild cognitive impairment and Alzheimer's disease. J. Neurol. Neurosurg. Psychiatry 71:441–447.

Dubois, B., H. H. Feldman, C. Jacova, S. T. Dekosky, P. Barberger-Gateau, J. Cummings, et al. 2010. Revising the definition of Alzheimer's disease: a new lexicon. Lancet Neurol. 9:1118–1127.

Guo, X., Z. Wang, K. Li, Z. Li, Z. Qi, Z. Jin, et al. 2010. Voxel-based assessment of gray and white matter volumes in Alzheimer's disease. Neurosci. Lett. 468:146–150.

Hirata, Y., H. Matsuda, K. Nemoto, T. Ohnishi, K. Hirao, F. Yamashita, et al. 2005. Voxel-based morphometry to discriminate early Alzheimer's disease from controls. Neurosci. Lett. 382:269–274.

Karas, G. B., E. J. Burton, S. A. Rombouts, R. A. van Schijndel, J. T. O'Brien, P. Scheltens, et al. 2003. A comprehensive study of gray matter loss in patients with Alzheimer's disease using optimized voxel-based morphometry. Neuroimage 18:895–907.

Killiany, R. J., T. Gomez-Isla, M. Moss, R. Kikinis, T. Sandor, F. Jolesz, et al. 2000. Use of structural magnetic resonance imaging to predict who will get Alzheimer's disease. Ann. Neurol. 47:430–439.

Klunk, W. E., H. Engler, A. Nordberg, Y. Wang, G. Blomqvist, D. P. Holt, et al. 2004. Imaging brain amyloid in Alzheimer's disease with Pittsburgh Compound-B. Ann. Neurol. 55:306–319.

Madsen, S. K., A. J. Ho, X. Hua, P. S. Saharan, A. W. Toga, C. R., Jr. Jack, et al. 2010. 3D maps localize caudate nucleus atrophy in 400 Alzheimer's disease, mild cognitive impairment, and healthy elderly subjects. Neurobiol. Aging 31:1312–1325.

Ohnishi, T., H. Matsuda, T. Tabira, T. Asada, and M. Uno. 2001. Changes in brain morphology in Alzheimer disease and normal aging: is Alzheimer disease an exaggerated aging process? Am. J. Neuroradiol. 22:1680–1685.

Price, J. C., W. E. Klunk, B. J. Lopresti, X. Lu, J. A. Hoge, S. K. Ziolko, et al. 2005. Kinetic modeling of amyloid binding in humans using PET imaging and Pittsburgh Compound-B. J. Cereb. Blood Flow Metab. 25:1528–1547.

Shi, F., B. Liu, Y. Zhou, C. Yu, and T. Jiang. 2009. Hippocampal volume and asymmetry in mild cognitive impairment and Alzheimer's disease: meta-analyses of MRI studies. Hippocampus 19:1055–1064.

Sled, J. G., A. P. Zijdenbos, and A. C. Evans. 1998. A nonparametric method for automatic correction of intensity nonuniformity in MRI data. IEEE Trans. Med. Imaging 17:87–97.

Smith, S. M. 2000. Fast robust automated brain extraction. Hum. Brain Mapp. 17:143–155.

Talairach, J., and P. Tournoux. 1988. Co-planar stereotactic atlas of the human brain. Thieme Verlag, Stuttgart, Germany.

特集　精神科領域における最近のMRIの進歩

VSRAD®*

松田博史**

Key Words：MRI, voxel-based morphometry(VBM), VSRAD®, Alzheimer's disease, major depressive disorder

脳容積測定の変遷

生体の詳細な脳構造の容積測定は精神・神経疾患の早期診断や鑑別診断，および進行度評価に必須の診断法となりつつある．この容積測法として最もよく用いられている画像は，間隙のない1 mmぐらいの薄いスライス厚で撮像された3次元のT1強調のMRIである．この脳容積測定法には，脳解剖を熟知した上で用手的に行う方法がとられてきた．しかし，測定が比較的容易な海馬でさえ測定者によって値がかなり異なり，熟練度を必要とする上に測定時間もかかる．一方，今世紀に入ってからコンピュータによる自動的容積測定法も広く用いられるようになってきた．脳容積の絶対値測定法として最も汎用されているソフトウェアに，米国で開発されたFreeSurfer(http://surfer.nmr.mgh.harvard.edu/)がある．このソフトウェアを用いれば全脳領域の詳細な脳構造の容積や大脳皮質厚の測定値を得ることができる．海馬においては用手的な測定結果と0.8を超える相関係数が得られており，世界的な標準手法として用いられつつある．ただし，1症例の測定結果を得るためには十数時間要すること，脳実質の抽出が不良の場合には測定値の信頼性が落ちるので用手的な修正を加えなければならないこと，FreeSurferのバージョンや使用するコンピュータのOperating Systemにより測定結果が異なること，Linuxベースのソフトウェアであり Graphic User Interfaceも不備なこともありハンドリングが難解なことなど，日常臨床で用いられていくためにはいまだ多くのハードルがある．

Voxel-based morphometry

脳容積の絶対値測定ではなく統計学的な測定手法として広く普及している方法にvoxel-based morphometry(VBM)がある．VBMの概念は英国のAshburnerら[1]により提唱された．米国のMathWorks社が開発している数値解析ソフトウェアであるMatlab上で動くStatistical Parametric Mapping(SPM, http://www.fil.ion.ucl.ac.uk/spm/)でVBM処理が可能であり，世界中で広く用いられている．VBMでは，各個人の脳をすべて標準脳の形態に変換した上で，ボクセル単位で統計学的解析を行う．

VBM処理では組織分割と解剖学的標準化が重要である．組織分割とは，MRIを灰白質，白質，脳脊髄液のコンパートメントに自動的に分割することである．この分割においてはT1強調像の信号値分布と，脳の位置ごとに灰白質，白質，脳脊髄

* Progress of recent MRI in psychiatry, VSRAD®.

** Hiroshi MATSUDA, M.D.: 独立行政法人国立精神・神経医療研究センター脳病態統合イメージングセンター〔〒187-8551 東京都小平市小川東町4-1-1〕; Integrative Brain Imaging Center, National Center of Neurology and Psychiatry, Kodaira, Tokyo 187-8551, Japan.

液のどの組織に属する可能性が高いかという情報である事前確率マップに基づいて，各ボクセルがそれぞれの組織をどれくらい含むかが算出される．事前確率マップは標準脳画像の上に定義されているため，このマップを被検者画像の形状に合わせる処理が必要となる．組織分割精度で問題となるのは，頭蓋骨の板間層や静脈，および白質の低信号領域などの灰白質と似た信号値を呈する組織が灰白質と誤認されうることである．この誤認を防ぐために行われてきた方法にoptimized VBMがある[2]．この方法では，まず，MRIの組織分割を被検者脳上で行い，得られた灰白質成分画像を灰白質のテンプレートを用いて解剖学的標準化を行う．この解剖学的標準化に用いられた変形パラメータをMRIの原画像に応用し解剖学的標準化を再度行う．この後，標準脳図譜上で再度，組織分割を行うことにより，精度の高い組織分割を行う手法である．最近では，このoptimized VBMのサイクリックな処理過程を一つの処理としてまとめ，さらに信号値の不均一性補正も強化されたunified segmentation手法がSPMで多用されるようになってきている．SPMのunified segmentationはFMRIB's Software LibraryやFreeSurferなど他の画像解析ソフトウェアよりも分割精度に優れることが報告されている[3]．

解剖学的標準化においては，従来のSPMではテンプレートに対して離散コサイン変換が用いられてきたが，最近では，より正確な標準化が可能なdiffeomorphic anatomical registration using exponentiated Lie algebra(DARTEL)[4]と呼ばれる非線形変換がSPMに応用されている．この非線形変換は，他の画像解析ソフトウェアよりも変換精度に優れており[5]，灰白質のみならず，白質画像も精度良く標準脳に変換できる．このため，離散コサイン変換では脳溝の開大などが存在する場合にテンプレートへの形態変換が不十分なために萎縮と評価されやすい灰白質もDARTELでは正確に容積を評価できるようになった．また，離散コサイン変換では困難であった脳室拡大における白質の解剖学的標準化もDARTELではほぼ正確に行うことができる．このようにDARTELによれば，解剖学的構造の個人差の影響を受けにくく，灰白質や白質容積そのものをより忠実に比較しうる．複雑なDARTEL解析を一連の処理として行うことのできるSPMのtoolboxとして，VBM8 toolbox (http://dbm.neuro.uni-jena.de/vbm8)があり，横断のみならず縦断解析にもSPM8とDARTELを用いることができる．

VSRAD®の開発

われわれは，ロンドン大学の許可のもとに，Matlabを用いずにWindows PC上で単独で作動するVBMのフリーソフトウェアとして，Voxel-based Specific Regional analysis system for Alzheimer's Disease(VSRAD®)を開発した．VSRAD®は，あらかじめ搭載された54～86歳の健常者80例からなる脳画像データベースと統計学的に比較することにより，個々の患者の局所脳容積を評価するためのSPMを応用したフリーソフトウェアである．2005年に最初のバージョンが開発され[6]，2009年に表示系が改善されたVSRAD®plus, 2012年に処理過程が大幅に改善されたVSRAD®advanceがリリースされた[7]．本邦で2,000以上の施設で用いられており，MRIによる萎縮評価の自動診断が行われている．VSRAD®advanceはSPM8とDARTEL手法を組み合わせたものである．処理フローを図1に示す．組織分割を行い，解剖学的標準化を行った後には，等方性の8 mm立方の平滑化を行うことにより，脳機能局在の個人差をより少なくするとともに，信号対雑音比を向上させ，さらに画像の計数率分布を正規分布に近づける．健常者の画像データベースとの統計検定においては，画像データベースの平均画像と標準偏差画像を用いて脳局所ごとに個々の患者の灰白質や白質容積が健常者の平均容積から何標準偏差離れているかを示すZスコアを算出し，カラースケールマップとして標準脳上または被検者脳上に表示している(図2, 3)．検定範囲は，あらかじめ設定された灰白質や白質のマスク画像の重畳により一定の領域となっている．

VSRAD®advanceでは，アルツハイマー病初期の患者群と年齢をマッチさせた健常高齢者群のSPMによる群間解析結果から嗅内皮質，扁桃，海馬を含む内側側頭部に標的関心領域を決定している．この標的関心領域から以下の4つの指標を算出している(図4)．

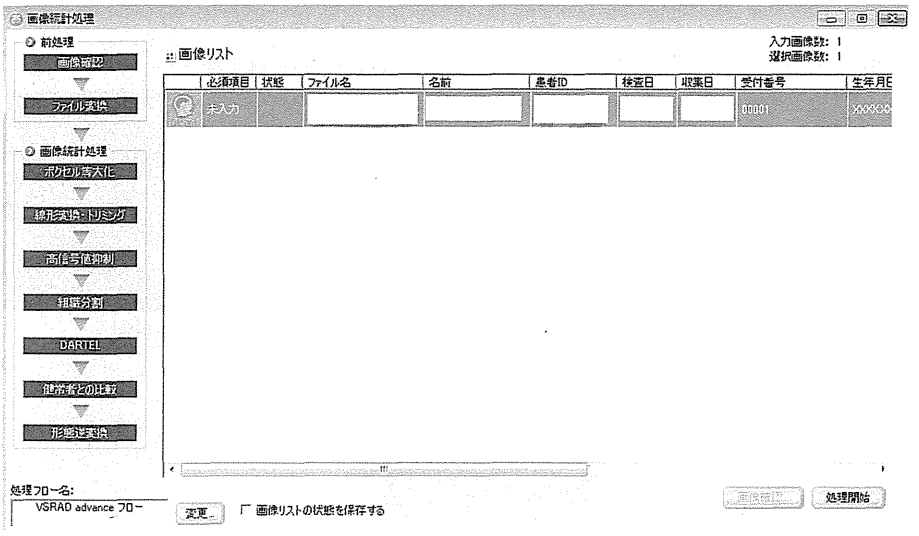

図1　VSRAD®advanceの処理フロー
複数例の自動解析も可能である．1例につき10分程度で解析できる．

①萎縮度：標的関心領域内の正のZスコアの平均値．

VSRAD®advanceでは最も標準的な指標である．目安であるが，0～1はほとんど萎縮がみられない．1～2は萎縮がややみられる．2～3は萎縮がかなりみられる．3以上は萎縮が強いといえる．

②萎縮領域の割合：標的関心領域内で2以上のZスコアがみられる割合．

目安であるが，0～30%が萎縮している体積が狭い，30～50%が萎縮している体積がやや広い，50%以上が萎縮している体積が広いといえる．

③全脳の萎縮領域の割合：全脳で2以上のZスコアがみられる割合．

目安であるが，10%以上が脳全体の萎縮が強いといえる．

④萎縮比：標的関心領域の萎縮割合と脳全体の萎縮割合の比．

標的関心領域が全脳に比べて，どれだけ特異的に萎縮しているかを表す．アルツハイマー病では，内側側頭部領域が全脳に比べて選択的に萎縮しているので，この指標は他の認知症性疾患との鑑別に役立つ．目安であるが，0～5は選択性があるとはいえない，5～10は選択性がみられる，10以上は選択性が強いといえる．

VSRAD®advanceにおいて，通常は灰白質や白質容積の全脳平均を一定の値に固定して正規化

図2　VSRAD®advanceの処理結果表示ボタン
萎縮の相対評価のみならず絶対評価も灰白質および白質で可能である．

することにより評価している．この正規化により，同じMRI装置を用いたとしても撮像日の違いによる測定誤差やMRI装置の違いによる測定誤差を抑えることができる．また，アルツハイマー病における内側側頭部に置かれた標的関心領域の萎縮度，萎縮領域の割合，全脳の萎縮に比べて標的関心領域の萎縮がいかに高度化を示す萎縮比がこの正規化により上昇する．特に萎縮比

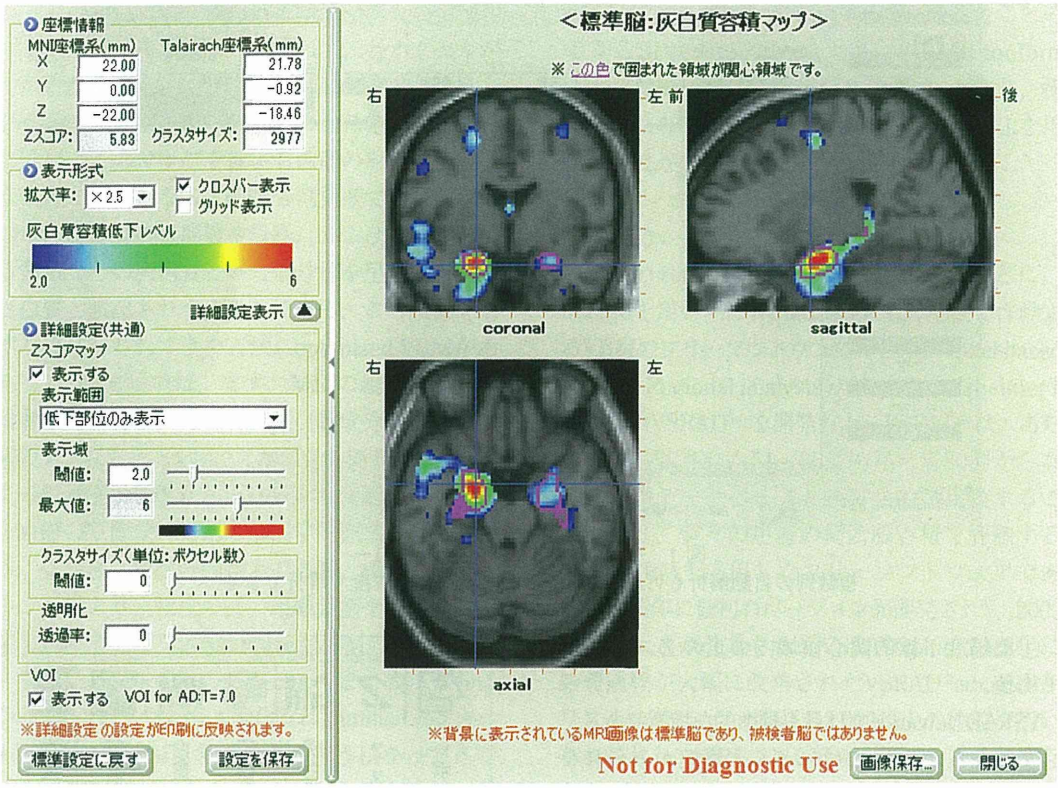

図3　標準脳上でのZスコアマップ表示
紫色の線で囲まれた範囲がアルツハイマー病で最も萎縮がみられる領域を示す.

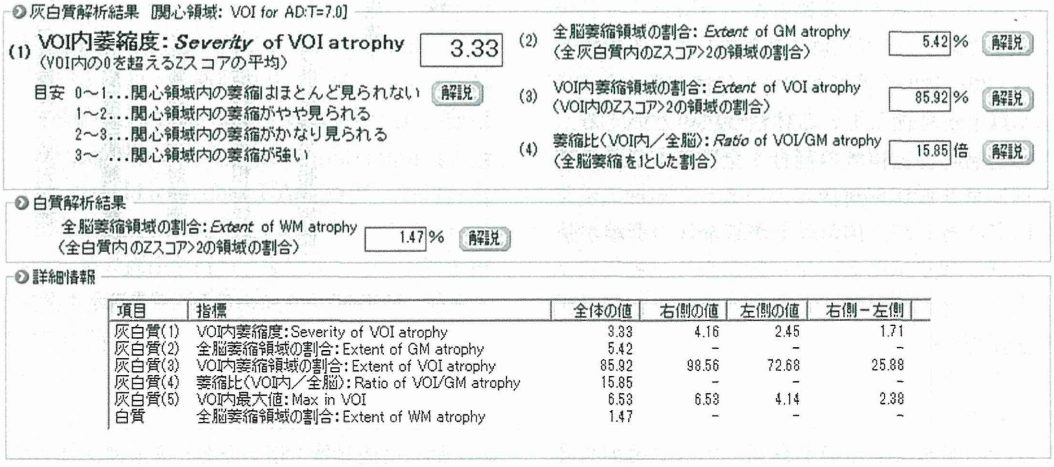

図4　Zスコア解析結果
標的関心領域における灰白質の萎縮指標および全脳における灰白質と白質の萎縮指標を得ることができる.

は2.5倍程度上昇し，他の認知症性疾患との鑑別が容易になる．健常高齢者とアルツハイマー病のごく初期の患者との識別も，正規化により10%程度向上する．

灰白質濃度の正規化により，目で見た萎縮とVSRAD®advance解析結果が異なる場合がある．

表1 VSRAD®advanceによる健常高齢者とアルツハイマー型認知症における解析値

グループ	標的関心領域(内側側頭部)			全脳の萎縮領域の割合(%)
	萎縮度	萎縮領域の割合(%)	萎縮比	
・高齢健常者	0.7±0.3	2.0±4.9	1.3±2.8	1.4±0.9
・アルツハイマー型認知症				
ごく初期	2.2±0.9	49.2±30.2	12.9±7.8	4.1±2.5
初期	2.7±0.8	63.7±25.8	15.4±7.8	4.3±1.9
中期から後期	3.0±1.0	68.7±24.1	11.7±6.7	7.1±3.7

平均±標準偏差

すなわち，内側側頭部の萎縮がみられたとしても全脳の萎縮がより高度であれば，低いZスコアの値しか得られない．このときの萎縮比は低値になるので，アルツハイマー病らしさは低くなる．逆に，目で見て内側側頭部の萎縮はごく軽度なのに高いZスコアを示す例がある．この場合には全脳の萎縮がほとんど存在しないことになり，ごく初期のアルツハイマー病の病態をみている可能性がある．

注意しなければならない点として，患者の年齢がある．VSRAD®advanceの健常者の正常データベースの年齢よりも極端に若い患者を解析対象とした場合に高いZスコアが得られることがある．この理由は，正常な加齢変化における内側側頭部の萎縮の進行は他の全脳領域よりも遅いことが知られており，高齢者ほど内側側頭部容積が相対的に保たれる傾向にあるためである．言い換えると，若年者では内側側頭部容積は他の脳部位に比べ相対的に低いため，高齢者のデータベースと比較すると高い値が出ることになる．

VSRAD®plusまでの古いバージョンでは，解析結果と画像所見が乖離する例がVSRAD®advanceよりも多くみられた．よくみられた事例としては，シルビウス裂や第3脳室が高度に拡大した場合，解剖学的標準化が不十分のために位置ずれが起きる．このため，前方の内側側頭部の容積を過小評価し，結果として高いZスコアがみられるというものであった．また，篩骨洞の空気と接する前頭葉底面では磁化率アーチファクトにより信号値が高くなることがある．この現象により灰白質が白質と間違えられて分割化され，灰白質濃度が低下する．VSRAD®plusまでは，標的関心領域がVSRAD®advanceよりも前方に設置されていたことにより，ときにこのアーチファクトの影響を受けて高いZスコアが出ることがあった．

灰白質や白質容積の全脳平均値による正規化の欠点は，全脳でびまん性に萎縮が起きた場合に全脳の萎縮領域の割合を過小評価してしまうことである．この過小評価を避けるために，VSRAD®advanceでは，灰白質や白質容積の総量を維持する方法(modulation)により容積の絶対値を評価することができる．たとえば，萎縮している海馬をテンプレートに完璧に合わせこんだ場合に，テンプレートの海馬と同じ大きさまで大きくなるが，灰白質の総量が維持されることで海馬のボクセル値が低下することになり，容積の絶対値を表現することができる．ただし，この絶対値測定は，MRI装置の違いなどによる測定誤差を受けやすいことに留意しなければならない．

VSRAD®advanceでの解析結果を検討する際には，再現性も認識しておかなければならない．同じ人が異なるMRI装置で撮像した場合，VSRAD®advanceで得られるZスコアには平均で10%前後の誤差が生ずる．また，同じMRI装置を用いたとしても，撮影日を変えた測定値間で，萎縮度は0.01±0.08(平均±標準偏差)，萎縮領域の割合は0.2±1.9%，萎縮比は0.01±0.87と変動する．

健常者とアルツハイマー病におけるVSRAD®advanceから求められた萎縮指標を表1に示す．VSRAD®advanceは，アルツハイマー病の早期診断および経過観察に有用性が高い(図5)．

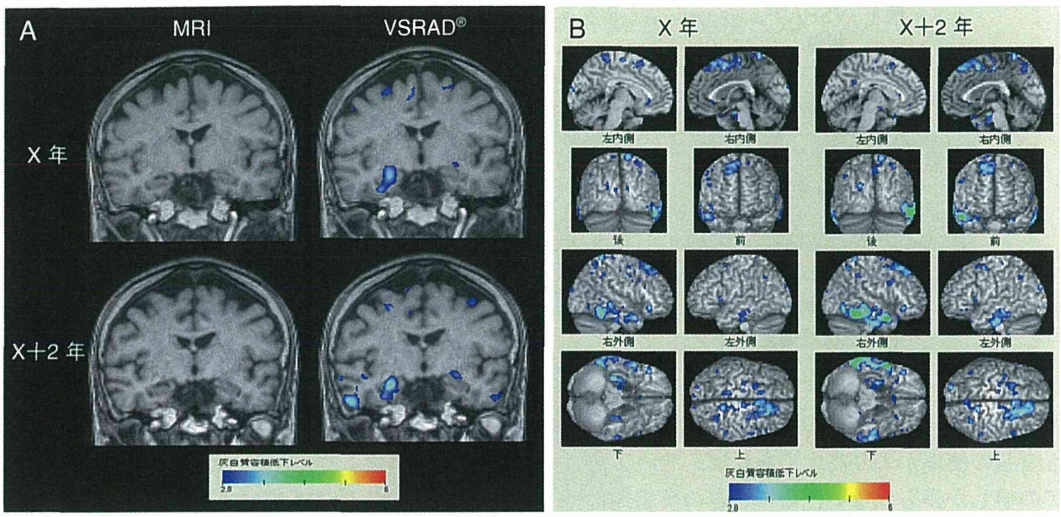

図5　60歳代前半女性，初期アルツハイマー病の縦断解析

A：軽度認知障害の段階(X年，Mini-Mental State Examinationスコアで24点)の冠状段像で内側側頭部の萎縮を判定することはできない．VSRAD®advanceでは，右内側側頭部の萎縮を示すカラーマップが得られている．2年後(X+2年，Mini-Mental State Examinationスコアで19点)では，右内側側頭部の萎縮が進行している．B：標準脳の脳表表示においてX年からX+2年の間に，中側頭回から下側頭回において右優位の萎縮の進行がみられる．

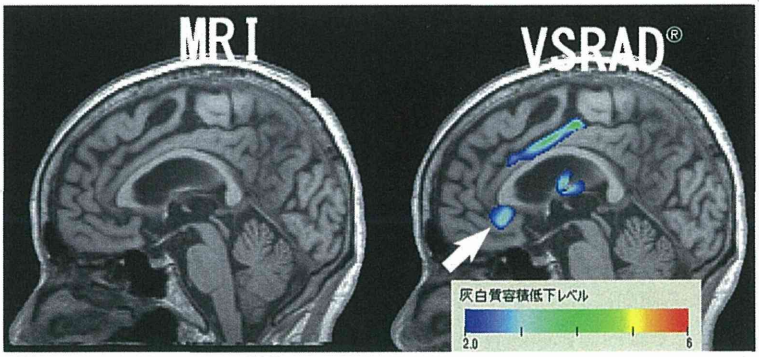

図6　大うつ病への応用

70歳代後半女性の大うつ病患者におけるVSRAD®advanceによるVBM解析．矢印で示す吻側の前部帯状回に，統計学上有意の萎縮を示すZスコアのカラーマップがみられる(矢印)．MRIの原画像で異常は指摘できない．
(南斗クリニック・仁井田りち先生，友愛会南部病院・仁井田　明先生ご提供)

VBMの大うつ病への応用

VBMの有用性が期待される精神疾患として，大うつ病があげられる．高齢者うつ病は認知症との鑑別が重要であるが，うつ病から認知症への移行も少なくなく，また認知症においてもうつ症状がみられる．高齢者のうつは，アルツハイマー型認知症や血管性認知症と相互に関連した病態と考えられており，症状のみから，大うつ病と認知症を鑑別することはしばしば困難である．この鑑別のためにVBMが期待される．

最近のメタアナリシスでは，VBMを用いた過去の23論文での986症例が対象とされている[8]．その結果，最も一貫して限局性に萎縮がみられる領域は，吻側の前部帯状回であり，Brodmann領野では32野および24野に相当する．うつ状態の重症度とこの領域の萎縮程度に関連はみられないとする報告が多い．吻側の前部帯状回は実

行抑制，悲しみの誘導，および否定的感情の処理などに関連する．この部位の容積低下は神経膠細胞密度の減少や神経細胞の縮小を意味し，ストレス系である視床下部－下垂体－副腎皮質系の機能異常をひき起こす可能性がある．さらにこの領域は眼窩前頭皮質，扁桃体，前部島皮質と広範囲に結合し，感情認識および感情制御の重要な拠点である．このように，吻側の前部帯状回の容積低下の検出は大うつ病への脆弱性を示す生物学的マーカとなりうる可能性を秘めている．Niidaら[9)10)]は，大うつ病の診断におけるVSRAD®の正診率が90％近いと報告しており（図6），今後の複数施設での検討が待たれる．

文　献

1) Ashburner J, Friston KJ. Voxel-based morphometry—the methods. Neuroimage 2000 ; 11 : 805-21.
2) Good CD, Johnsrude IS, Ashburner J, et al. A voxel-based morphometric study of ageing in 465 normal adult human brains. Neuroimage 2001 ; 14 : 21-36.
3) Eggert LD, Sommer J, Jansen A, et al. Accuracy and reliability of automated gray matter segmentation pathways on real and simulated structural magnetic resonance images of the human brain. PLoS One 2012 ; 7 : e45081.
4) Ashburner J. A fast diffeomorphic image registration algorithm. Neuroimage 2007 ; 38 : 95-113.
5) Klein A, Andersson J, Ardekani BA, et al. Evaluation of 14 nonlinear deformation algorithms applied to human brain MRI registration. Neuroimage 2009 ; 46 : 786-802.
6) Hirata Y, Matsuda H, Nemoto K, et al. Voxel-based morphometry to discriminate early Alzheimer's disease from controls. Neurosci Lett 2005 ; 382 : 269-74.
7) Matsuda H, Mizumura S, Nemoto K, et al. Automatic voxel-based morphometry of structural MRI by SPM8 plus diffeomorphic anatomic registration through exponentiated lie algebra improves the diagnosis of probable Alzheimer Disease. AJNR Am J Neuroradiol 2012 ; 33 : 1109-14.
8) Bora E, Fornito A, Pantelis C, et al. Gray matter abnormalities in major depressive disorder : a meta-analysis of voxel based morphometry studies. J Affect Disord 2012 ; 138 : 9-18.
9) Niida R, Niida A, Motomura M, et al. Diagnosis of depression by MRI scans with the use of VSRAD—a promising auxiliary means of diagnosis : a report of 10 years research. Int J Gen Med 2011 ; 4 : 377-87.
10) Niida A, Niida R, Matsuda H, et al. Identification of atrophy of the subgenual anterior cingulate cortex, in particular the subcallosal area, as an effective auxiliary means of diagnosis for major depressive disorder. Int J Gen Med 2012 ; 5 : 667-74.

*　　*　　*

MRIによる脳容積測定

松田博史

国立精神・神経医療研究センター 脳病態統合イメージングセンター

はじめに

生体の詳細な脳構造の容積測定は認知症の早期診断や鑑別診断、および進行度評価に必須の診断法である。この容積測定においてもっともよく用いられている画像は、間隙のない1mmぐらいの薄いスライス厚で撮像された3次元のT1強調のMRIである。この脳容積測定法には、脳解剖を熟知した上で用手的に対象構造をトレーシングする方法がとられてきた。しかし、構造の識別が比較的容易な海馬でさえ時間がかかるうえに、測定者によっても値がかなり異なる。このために、欧州を中心にHarmonized Protocolとしてトレーシング法の標準化が行われている(http://www.hippocampal-protocol.net/SOPs/index.html)。

一方、今世紀にはいってからコンピュータによる自動的容積測定法も盛んに用いられるようになってきた。脳容積の絶対値測定法としてもっとも汎用されているソフトウェアに、米国で開発されたFreeSurfer (http://surfer.nmr.mgh.harvard.edu/)がある。このソフトウェアを用いれば、アルツハイマー病で最初に脳萎縮がみられるとされる嗅内皮質や海馬の容積が自動的に算出されるのに加え、全脳領域の詳細な容積測定値や皮質厚を得ることができる(図1)。海馬においては用手的な測定結果と0.9を超える相関係数が得られており(図2)、世界的な標準手法として用いられつつある。ただし、1症例の測定結果を得るためには、最新バージョンのFreeSurfer 5.2においてGPUを応用しても数時間要すること、脳実質の抽出が不良の場合には測定値の信頼性が落ちるので用手的な修正を加えなければならないこと、FreeSurferのバージョンや使用するコンピュータのOperating Systemにより測定結果が異なること、Linuxベースのソフトウェアであり Graphic User Interfaceも不備なこともありハンドリングが難解なことなど、日常臨床で用いられていくためには未だ多くのハードルがある。

Voxel-based morphometry

脳容積の絶対値測定ではなく、統計学的な測定手法として広く普及している方法にVoxel-based morphometry (VBM)がある。VBMの概念は英国のAshburnerらにより提唱された。米国のMathWorks社が開発している数値解析ソフトウェアであるMatlab上で動くStatistical Parametric Mapping (SPM)でVBM処理が可能であり、世界中で広く用いられている。

VBM処理では組織分割と解剖学的標準化が重要である。組織分割とは、MRIを灰白質、白質、脳脊髄液のコンパートメントに自動的に分割することである。この分割においてはT1強調像の信号値分布と、脳の位置ごとに灰白質、白質、脳脊髄液のどの組織に属する可能性が高いかという情報である事前確率マップに基づいて、各ボクセルがそれぞれの組織をどれくらい含むかが算出される。事前確率マップは標準脳画像の上に定義されているため、このマップを被検者画像の形状に合わせる処理が必要となる。この分割精度で問題となるのは、頭蓋骨の板間層や静脈、および白質の低信号領域などの灰白質と似た信号値を呈する組織が灰白質と誤認されうることである。SPMで用いられているunified segmentationなどの手法